Liquid Crystals
Publication details, including instructions for authors and subscription information:
http://www.informaworld.com/smpp/title~content=t713926090

Microscopic organization of molecules in smectic A and chiral (racemic) smectic C phases: Dynamic molecular deformation effect on the S_A to S_C^* (S_C) transition

Atsushi Yoshizawa[a]; Hiroshi Kikuzaki[b]; Mitsuo Fukumasa[a]
[a] Petroleum Laboratory, Saitama, Japan [b] Analytical Research Centre, Japan Energy Corporation 3-17-35, Saitama, Japan

To cite this Article Yoshizawa, Atsushi , Kikuzaki, Hiroshi and Fukumasa, Mitsuo(1995) 'Microscopic organization of molecules in smectic A and chiral (racemic) smectic C phases: Dynamic molecular deformation effect on the S_A to S_C^* (S_C) transition', Liquid Crystals, 18: 3, 351 — 366
To link to this Article: DOI: 10.1080/02678299508036633
URL: http://dx.doi.org/10.1080/02678299508036633

LIQUID CRYSTALS, 1995, VOL. 18, NO. 3, 351–366

Microscopic organization of molecules in smectic A and chiral (racemic) smectic C phases: Dynamic molecular deformation effect on the S_A to S_C^* (S_C) transition

by ATSUSHI YOSHIZAWA*†, HIROSHI KIKUZAKI‡ and MITSUO FUKUMASA†

† Petroleum Laboratory and ‡ Analytical Research Centre, Japan Energy Corporation 3-17-35, Niizo-minami, Toda-shi, Saitama 335, Japan

(*Received 15 November 1993; accepted 1 March 1994*)

We investigated the correlation between orientational order and microscopic organization of the molecules in smectic A and chiral (racemic) smectic C phases by means of solid-state C-13 NMR, powder X-ray diffraction, and electrooptical measurements. The compounds under investigation are 4-((*S*)-2-methyloctanoyl)phenyl 4′-nonylbiphenyl-4-carboxylate ((*S*)-MONBIC) and its corresponding racemic compound ((*S*, *R*)-MONBIC). Static C-13 NMR indicates that: (1) the orientational angle of the tail with respect to the magnetic field decreases slightly both in the S_A and S_C^* phases as decreasing temperature, and (2) the angle of the core with respect to the field decreases in the S_A phase but increases in the S_C^* phase as decreasing temperature. Analysis of C-13 T_1 reveals that the dynamic molecular deformation for the core part can occur near the transition. We discuss the dynamic molecular deformation in comparison with the reorientation of the director at the S_A to S_C^* transition. Based on the experimental results, we propose the structural model in which describes the microscopic organization of the molecules in the mesophases.

1. Introduction

Smectic liquid crystals [1] have attracted much attention due to their characteristic molecular assembly and their applications in electro-optical devices. Recently important discoveries concerning chiral smectic liquid crystal phases—ferroelectric phases [2], 'Abrikosov' type twist grain boundary (TGB) phases [3], and antiferroelectric phases [4]—have been reported. Experimental and theoretical works have been performed to understand the appearance of these chiral smectic phases [5–10]. Nevertheless, some basic problems seem to still remain. The smectic A, smectic C, the ferroelectric chiral smectic C phases have the general structure shown in figure 1. In the S_A phase, though locally tilted, the average direction of the molecules is parallel to the layer normal. In the S_C phase, the molecules are tilted with respect to the layer normal and the tilt direction is constant over considerable volume elements. In the S_C^* phase, the molecules are tilted with respect to the layer normal and form a helical distribution on moving from layer to layer. Ferroelectricity appears in the S_C^* phase. In the tilted smectic phases, the origin of the long range correlation of the tilt direction is not understood very well. Why is the tilt direction constant in the S_C phase? Why is the helical distribution of the tilt direction formed in the S_C^* phase? In order to explain the physical properties of smectic phases, the orientation and dynamics of a director are discussed by using a rod model [11] and the correlation between physical properties and molecular structure is investigated. It seems to be important to understand the correlation between orientational order in the smectic phases and the microscopic organization of the

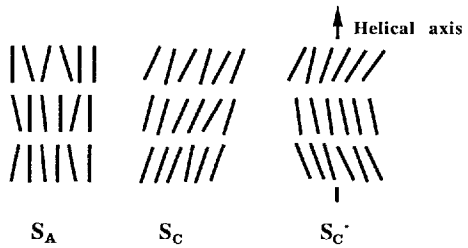

Figure 1. Structure of the smectic A (S_A), smectic C (S_C), and chiral smectic C (S_C^*) phases.

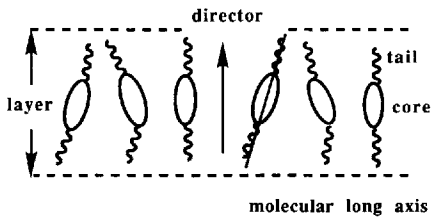

Figure 2. The schematic relationships among molecule, molecular long axis, and director.

* Author for correspondence.

molecules in the mesophases. Figure 2 shows the schematic relationships among the molecule, the molecular long axis, and the director in the S_A phase. The molecular long axis represents the pseudo-symmetry axis of the molecule. The molecule is assumed to rotate around its long axis. The director is a unit vector parallel to the average direction of molecular long axes. Typical motions in the S_C^* phase are fast internal motion, fast overall motions (as in the rotation around the molecular long axis or the reorientation of the long axis), fluctuation of the molecule with the orientational angle between the layer normal and the director (soft mode [12]), slow fluctuation of the molecule around the cone (Goldstone mode [12]), and slow fluctuation of the director. The behaviour of the molecules in the mesophases depends on the molecular structure. C-13 NMR provides useful information about orientation and motion of an individual molecule in liquid crystal phases via the molecular structure [13–15]. We have investigated the phase transitions in ferroelectric [16, 17] and antiferroelectric [18] liquid crystals by means of solid-state C-13 NMR.

We report here on the investigation of the S_A to S_C^* (or S_C) transitions of oriented and non-oriented smectic liquid crystals by means of solid-state C-13 NMR. The results of NMR measurements are compared with those of electro-optical and X-ray measurements. Analysis of spin–lattice relaxation times reveals dynamic behaviour of the molecules at the S_A to S_C^* transition. We discuss the orientation and motion of an individual molecule in comparison with the orientation of the director and present a possible S_A to S_C^* transition model.

2. Experimental

2.1. *Materials*

Two liquid crystals reported by us were used for the measurements. One of them is optically active 4-((*S*)-2-methyloctanoyl)phenyl 4′-nonylbiphenyl-4-carboxylate ((*S*)-MONBIC) prepared from (*S*)-2-methyloctanoic acid (Japan Energy Corporation, 89 per cent enantiomer excess). The structural formula of (*S*)-MONBIC is given in figure 3. The reasons for choosing (*S*)-MONBIC for the measurements are (*a*) favourable temperature range and (*b*) the large spontaneous polarization in the S_C^* phase. The other compound is the corresponding racemic compound ((*S*,*R*)-MONBIC) prepared from the racemic 2-methyloctanoic acid.

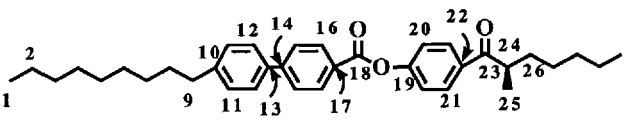

Figure 3. The structure formula of (*S*)-MONBIC. The carbon atoms of (*S*)-MONBIC are numbered as shown in the figure.

2.2. *Synthesis*

2.2.1. *4-((S)-2-Methyloctanoyl)phenol*

Commercially available (*S*)-2-methyloctanoic acid (89 per cent ee, Japan Energy Corporation) was used as the starting material. We added (*S*)-2-methyloctanoic acid (8·93 g, 56·4 mmol) to thionyl chloride (8·98 g, 75·5 mmol). The mixture was stirred at room temperature for 1 h and then 70°C for 2 h. The excess thionyl chloride was removed. The (*S*)-2-methyloctanoyl chloride (9·80 g, 55·5 mmol, 98 per cent) was obtained.

Into a flask charged with methoxybenzene (1·23 g, 11·4 mmol), was dissolved 5 ml of dry dichloromethane. To this solution we added dropwise a solution of (*S*)-2-methyloctanoyl chloride (2·03 g. 11·5 mmol) and aluminium chloride (1·75 g, 13·1 mmol) in dry dichloromethane at 0°C over 10 min. The reaction mixture was then stirred at room temperature for 14 h. The reaction mixture was then poured into 50 ml of ice water and extracted with dichloromethane (2 × 20 ml). The combined organic layers were washed with water (40 ml) and dried over anhydrous magnesium sulphate. The drying agent and solvent were removed and the residue was purified by column chromatography on silica gel using toluene as eluent. 1·84 g (7·05 mmol, 65 per cent) of 4-methoxy-4′-((*S*)-2-methyloctanoyl)benzene was obtained. IR (neat) 2920, 1670, 1595, 1250, 1230, 1170, cm^{-1}; $[\alpha]_D^{25}$ + 1·3° (neat).

2·03 g (8·2 mmol) of the above 4-methyloxy-4′-((*S*)-2-methyloctanoyl)benzene was dissolved in 15 ml of dry toluene in a flask. Aluminium bromide (6·64 g, 24·9 mmol) was added to the solution under ice cooling. The reaction solution was then stirred at room temperature for 3 h. The reaction mixture was poured into ice water (100 ml) and extracted with toluene (2 × 40 ml). The combined organic layers were washed with water (2 × 50 ml) and dried over anhydrous magnesium sulphate. Column chromatography on silica gel using toluene as eluent and then using a 5 : 1 toluene/ethylacetate as an eluent produced 4-((*S*)-2-methyloctanoyl)phenol (1·88 g, 8·0 mmol, 98 per cent). ^{1}H NMR (90 MHz, $CDCl_3$) δ 8·2–7·9 (broad, 1 H), 8·0 (d, 2H), 7·0 (d, 2H), 3·4 (m, 1 H), 1·9–1·2 (m, 13 H), 0·9 (t, 3 H); IR (neat) 3250, 1650, 1580 cm^{-1}; $[\alpha]_D^{25}$ + 27·4° (*c* 10, $CHCl_3$).

2.2.2. *4-((S)-2-methyloctanoyl)phenyl 4′-nonylbiphenyl-4-carboxylate ((S)-MONBIC)*

A solution of 4′-nonylbiphenyl-4-carboxylic acid (500 mg, 1·5 mmol, Teikoku Kagaku Industry Co., Ltd.), 4-((*S*)-2-methyloctanoyl)phenol (270 mg, 1·2 mmol), *N*,*N*′-dicyclohexylcarbodiimide (300 mg, 1·5 mmol), and 4-dimethylaminopyridine in dichloromethane (10 ml) was stirred at room temperature for 10 h. After filtration to remove the precipitate, filtrate was concentrated. The

Table 1. Transition temperatures (°C) and enthalpies (kJ mol^{-1}) determined by DSC for (*S*)- and (*S*,*R*)-MONBIC.

Compound	C		S_3†		$S_C^*(S_C)$†		S_A		I
(*S*)-MONBIC	•	79			•	101	•	118	•
ΔH		25·6						4·9	
(*S*,*R*)-MONBIC	•	70	(•	48)	•	102	•	119	•
ΔH		27·0	(	2·3)				5·7	

† A higher ordered smectic phase not yet identified.
‡ Transition enthalpies of the S_A–S_C^* for (*S*)-MONBIC and the S_A–S_C for (*S*,*R*)-MONBIC were too small to be evaluated.

residue was purified by column chromatography on silica gel using toluene as eluent followed by recrystallization from ethanol. 350 mg (0·65 mmol, 57 per cent) of the desired product was obtained. ^{1}H NMR (90 MHz, $CDCl_3$) δ 8·3–7·2 (12 H), 3·45 (m, 1 H), 2·65 (t, 2 H), 1·9–1·2 (m, 27 H), 0·9 (t, 6 H); IR (KBr) 2950, 2850, 1735, 1675, 1600 cm^{-1}. $[\alpha]_D^{25}$ +4·6° (*c* 5·0, $CHCl_3$).

(*S*,*R*)-MONBIC was prepared from the racemic (±)-2-methyloctanoic acid in a similar method to that for (*S*)-MONBIC.

2.3. *Measurements*

The phase transition temperature and enthalpies were determined by differential scanning calorimetry (DSC) using a Seiko DSC-200 calorimeter. The liquid crystal transition temperatures and the phase textures were also observed by thermal optical microscopy using a Nikon polarizing microscope equipped with a Mettler FP 82 hot stage in conjunction with FP 80 control unit. DSC and optical measurements were carried out at a scanning rate of 2·0°C min^{-1}. Cells (purchased from EHC Co., Ltd.) of 2·5 μm were used for measurements of the spontaneous polarization and tilt angle. The cells were constructed from the ITO-coated glass with polyimide film rubbed in one direction. The spontaneous polarization was measured by the triangular wave method [19] and the tilt angle was derived from optical switching angle of the sample. Powder X-ray diffraction patterns were obtained using a Rigaku RAD-IIB. C-13 NMR measurements both with rapid sample spinning and without sample spinning were carried out using a JEOL GSX-270 spectrometer at 67·9 MHz with proton dipolar decoupling. Static C-13 NMR spectra were obtained without magic angle spinning (MAS). The sample was oriented by slow cooling from the isotropic liquid to the S_A phase in the super conducting magnet at 6·34 T. The cooling rate was approximately 1°C/15 min. The C-13 NMR spectra with MAS were observed at the spinning speed of 4·5 kHz. The temperature under the MAS condition was calibrated from the isotropic liquid to S_A and the S_A to S_C^* (or S_C) phase transitions of the samples. The measurements of C-13 spin-lattice relaxation time in the laboratory frame (T_1) both with MAS and without MAS were performed using 180°C–τ–90° pulse sequence. The measurements of C-13 spin-lattice relaxation time in the rotating frame ($T_{1\rho}$) with MAS were performed using the spin-locking method at the spin-locking frequency of 56 kHz.

3. Results and discussion

3.1. *DSC and X-ray measurements*

Table 1 shows transition temperatures and enthalpies for (*S*)-MONBIC and (*S*,*R*)-MONBIC determined by DSC measurements. The transition temperature from crystal to S_C^* was found to depend on the optical purity. Furthermore, the higher order smectic phase was observed only for the racemic compound.

Figure 4 shows powder X-ray diffraction patterns for (*S*)-MONBIC in the S_A, S_C^*, and crystal phases. X-ray patterns at small angles display a sharp Bragg reflection from smectic layers. The patterns at higher angles reflect the order inside the layer. In the S_A and S_C^* phases the peaks at higher Bragg angles remain diffuse, indicating that the order inside the layer is liquid-like in these phases [20]. In the crystal phase various combinations of sharp peaks are observed at higher angles. Figures 5 shows the temperature dependence of the layer spacing (*S*)-MONBIC obtained from the peaks at small angles. The layer spacing decreases from S_A to S_C^*, which indicates that the molecules are tilted in the S_C^* phase. The extended molecular length of (*S*)-MONBIC is estimated to be about 36 Å from a CPK model, which is longer than the layer spacing in the S_A phase determined by X-ray diffraction (32·5 Å). This difference can result from the orientational fluctuations of the molecules, the conformational distribution of the chains, the interdigitation, and the zig–zag molecular structure [21, 22]. The diffraction patterns of (*S*,*R*)-MONBIC in the S_A, S_C, and crystal phases were similar to those of (*S*)-MONBIC in the S_C^*, and crystal phases.

3.2. *Spontaneous polarization and tilt angle measurements*

The temperature dependence of spontaneous polarization observed for (*S*)-MONBIC and one to one mixture of

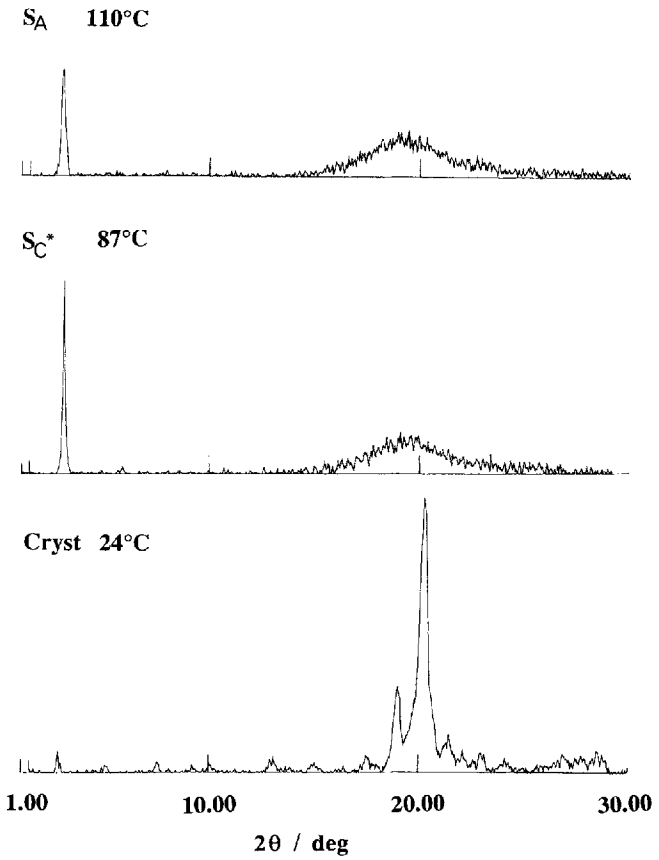

Figure 4. Powder X-ray diffraction patterns of (*S*)-MONBIC in the S_A, S_C^* and crystal phases.

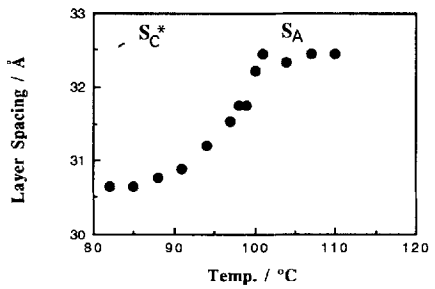

Figure 5. The temperature dependence of the layer spacing of (*S*)-MONBIC in the S_A and S_C^* phases.

(*S*)-MONBIC and (*S*,*R*)-MONBIC is shown in figure 6 (*a*). (*S*)-MONBIC shows high spontaneous polarization ($-100\,nC\,cm^{-2}$ at 10°C below the S_A–S_C^* transition temperature), which is caused by a coupling between the chiral group and the keto function [23]. The temperature dependence of tilt angle for those samples is shown in figure 6 (*b*). The magnitude of polarization depends on the optical purity. On the other hand, the tilt angle does not depend on the optical purity. The polarization direction in the S_C^* phase depends on the optical sense of the compound. The dependence of the polarization on optical purity suggests that the motions of an individual molecule of (*S*)-MONBIC in the S_C^* phase are similar to those of (*S*,*R*)-MONBIC in the S_C phase.

Tilt angles determined by optical microscopy and X-ray measurements are shown in figure 7. The tilt angle by X-ray measurements is estimated assuming that the ratio of the S_C^* to S_A layer spacing is proportional to the cosine of the S_C^* tilt angle. The difference in the tilt angle determined from these two techniques is not unusual [21, 22]. In optical measurements, the tilt angle reflects the tilt of the core part with delocalized electrons of a molecule. In X-ray measurements, the tilt angle reflects the tilt of the long axis, i.e. the average tilt of a molecule. Figure 7 suggests that the tilt angle of the core part is larger

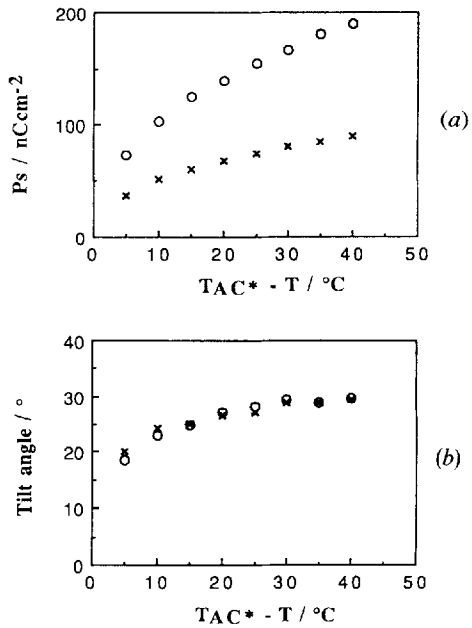

Figure 6. The temperature dependence of (*a*) the spontaneous polarization and (*b*) the tilt angle observed for (*S*)-MONBIC and one to one mixture of (*S*)-MONBIC and (*S*, *R*)-MONBIC. The circles show the values of (*S*)-MONBIC and the crosses show those of one to one mixture of (*S*)-MONBIC and (*S*, *R*)-MONBIC.

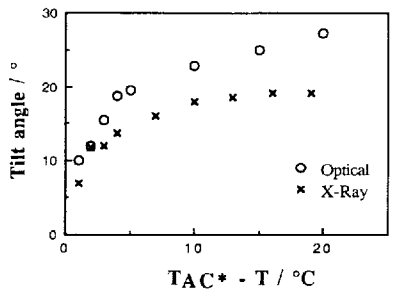

Figure 7. The temperature dependence of the tilt angle determined by optical microscopy and X-ray measurements.

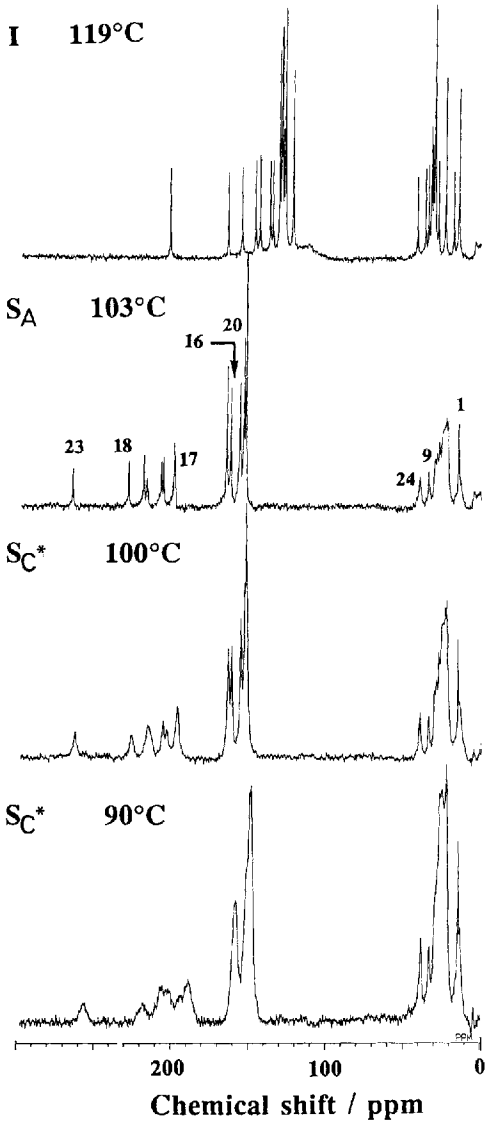

Figure 8. The C-13 NMR spectra of (*S*)-MONBIC in the isotropic liquid, S_A, and S_C^* phases without sample spinning. In the S_A phase, the peaks in the range from 197·1 to 217·2 ppm result from unprotonated-aromatic carbons and the peaks in the range from 151·5 to 163·8 ppm result from protonated-aromatic carbons.

than that of the long axis. We would like to confirm this suggestion by means of C-13 NMR in the following section.

3.3. *C-13 NMR measurements*

Figure 8 shows C-13 NMR spectra of (*S*)-MONBIC on cooling in the isotropic liquid, S_A, and S_C^* phases without MAS. Table 2 shows the observed chemical shifts of the typical carbons of (*S*)-MONBIC in the isotropic liquid, S_A and S_C^* phases. During the phase transition from isotropic liquid to S_A, C-13 chemical shifts of the keto, ester, and aromatic carbons increase markedly but those of the other aliphatic carbons decrease. These changes of the chemical shifts indicate that the molecules orient in such a way that the director is parallel to the direction of the external magnetic field. During the phase transition from S_A to S_C^*, the C-13 chemical shifts of the keto, ester and aromatic carbons decrease and those of the other aliphatic carbons also decrease slightly. The temperature dependence of chemical shifts observed for the tail and core carbons in the S_C^* phase indicates the difference in the orientation with respect to the field direction between the tail and the core in the S_C^* phase. The angle of the core part with respect to the magnetic field increases in the S_C^* phase as decreasing temperature. On the other hand, the angle of the tail with respect to the field decreases slightly in the S_A and S_C^* phases as decreasing temperature. The different tendency in the tilt between the core and the tail in the S_C^* phase observed by C-13 NMR is consistent with the difference in the tilt angle determined from X-ray and optical microscopy. The marked line broadening observed for the core (the keto, ester, and aromatic) carbons may be caused by the chemical shift anisotropy which depends on the helicoidal layer structure in the S_C^* phase [15]. Furthermore, the line broadening for the core and tail carbons seem to be affected by Goldstone mode related to the occurrence of ferroelectricity [24]. Near the S_A to S_C^* transition, there is difference in the temperature dependence of chemical shifts among the aromatic carbons (see table 2). From 106°C to 103°C in the S_A phase, the chemical shift (204·5 ppm) of unprotonated aromatic carbon not yet assigned does not change but those of the other unprotonated carbons increase. From 103°C in the S_A phase to 100°C in the S_C^* phase, the upfield shift (2·5 ppm) of the unprotonated carbon observed 204·5 ppm at 103°C is larger than that (1·8 ppm) of C_{17}. The different behaviour of chemical shifts among the aromatic carbons suggests the different tendency in the orientation with respect to the magnetic field among the phenyl rings of the core part near the transition. During the phase transition from S_A to S_C for (*S*,*R*)-MONBIC, however, C-13 chemical shifts of the keto, ester and aromatic carbons increase, but those of the other aliphatic carbons decrease (see figure 9) [17]. The lines for the core carbons of (*S*,*R*)-MONBIC in the S_C phase are broadened slightly compared with those of (*S*)-MONBIC in the S_C^* phase. The downfield shifts and slight line broadenings for the core carbons suggest that the director is oriented to the direction of magnetic field, whereas the layer normals are tilted in the S_C phase [14, 17, 25].

We estimate the order parameter of the molecular long axis of (*S*)-MONBIC roughly in the S_A phase from C-13 chemical shifts of the aromatic carbons. The chemical shift σ in an ordered liquid crystalline phase is related to the isotropic chemical shift σ_i, the components of the

Table 2. Observed chemical shifts† in the isotropic liquid (I), S_A, and S_C^* phases of (*S*)-MONBIC.

Temperature/°C		C_1	C_9	C_{16}	C_{17}	C‡	C_{18}	C_{20}	C_{23}	C_{24}
I	119	14·7	36·7	130·4	129·0	—	164·5	122·6	202·1	41·7
S_A	110	14·2	33·6	160·7	196·3	203·8	225·8	152·8	262·4	39·3
	106	14·2	33·5	161·2	197·0	204·5	226·7	152·9	263·3	39·2
	103	14·1	33·4	161·3	197·2	204·5	226·9	152·9	263·5	39·1
S_C^*	100	14·1	33·3	160·5	195·4	202·0	224·8	151·9	261·9	38·9
	94§	14·0	32·9	158·4	—	—	220·0	—	257·7	38·3
	90§	14·0	32·6	—	—	—	216·1	—	256·4	38·2

† Chemical shifts in ppm referenced to TMS.
‡ An unprotonated aromatic carbon not yet assigned.
§ The peaks for the aromatic carbons could not be assigned.

chemical shift tensor σ_{jk}, and the order parameters S_{jk} by equation (1) [26].

$$\sigma = \sigma_i + (2/3)S_{zz}\{\sigma_{zz} - (1/2)(\sigma_{xx} + \sigma_{yy})\} + (1/3)(\sigma_{xx} - \sigma_{yy})(S_{xx} - S_{yy}) + (2/3)S_{yz}\sigma_{yz} + (2/3)S_{xz}\sigma_{xz} + (2/3)S_{xy}\sigma_{xy}. \quad (1)$$

We assume that the bond angles of the molecule are the same as those determined for phenyl benzoate in the crystalline state [27]. Then a molecular long axis, *D*, which passes through the centres of the biphenyl rings and the phenyl ring, is defined as shown in figure 10. The ordering matrix of the molecule is assumed to be cylindrically symmetric around the molecular long axis so that equation (1) is reduced to

$$\sigma = \sigma_i + (2/3)S(\sigma_\parallel - \sigma_\perp), \quad (2)$$

where $\sigma_\parallel = \sigma_{zz}$ is the chemical shift component along the direction of the molecular long axis, $\sigma_\perp = (1/2)(\sigma_{xx} + \sigma_{yy})$ is the average of the components of the chemical shift tensor in the *xy* plane, and $S = S_{zz}$ is the order parameter associated with the long axis. *S* is defined as

$$S = \langle 3\cos^2\Theta - 1\rangle/2, \quad (3)$$

where Θ describes the orientation of the long axis with respect to the applied static magnetic field, and $\langle\ \rangle$ is a thermal average. For aromatic carbons, the magnetic equivalence of ortho aromatic carbon pairs indicates that the phenyl rings (rings I, II, and III in figure 10) of the core perform flips around each para axis. We can assume that fast molecular motions around the molecular long axis and fast 90° flips of phenyl rings around each para axis occur in the S_A phase. The chemical shifts of the aromatic carbons can be written for the ortho and meta carbons as [13]

$$\left.\begin{aligned}\sigma_\parallel &= (1/4)(1 + 2\sin^2\Phi)\sigma_{11} + (1/4)(1 + 2\cos^2\Phi)\sigma_{22},\\ \text{and}\\ \sigma_\perp &= (1/2)[(1/4)(1 + 2\cos^2\Phi)\sigma_{11} + (1/4)(1 + 2\sin^2\Phi)\sigma_{22} + \sigma_{33}],\end{aligned}\right\} \quad (4)$$

where Φ is the angle between the phenyl para axis and the molecular long axis. The order parameters can not be calculated from C-13 chemical shifts without precise values of the chemical shift tensors and the angles between the principal axes of the tensor and the molecular axes. However, both sets of data are difficult to measure. Therefore, we calculate values of *S* from certain core carbons (C_{16} and C_{20}) by using the principal values for the chemical shift tensors taken from model compounds [28–30]. Although the calculations of *S* may not be accurate, we can get rough values of *S* to estimate macroscopic ordering of MONBIC in the S_A phase. Shielding tensor elements used for C_{16} are $\sigma_{11} = -216$ ppm, $\sigma_{22} = -153$ ppm, and $\sigma_{33} = -15$ ppm [29], and those for C_{20} are $\sigma_{11} = -193$ ppm, $\sigma_{22} = -134$ ppm, and $\sigma_{33} = -12$ ppm [30]. According to figure 9, Φ is estimated to be 10° and 9° for the biphenyl (ring I and ring II) and the phenyl (ring III), respectively. The calculated order parameters from the chemical shifts of C_{16} and C_{20} at 103°C in the S_A phase are 0·75 and 0·83, respectively. By using the values of these order parameters, the thermal average of the orientational angle (Φ) in the S_A phase is estimated to be about 22°. In the case of the tail carbons, from isotropic liquid to S_A, the upfield shift of C_1 peak is smaller than that of C_9 peak. This suggests that the ordering fluctuations of the tail carbons are larger for the terminal of the tail and decrease on approaching the core along the tail.

C-13 T_1 measurements without MAS were performed for (*S*)-MONBIC. The obtained C-13 T_1 values are listed in table 3. The large downfield shifts and line broadenings for the unprotonated carbons and the aromatic carbons cause the large uncertainity for C-13 T_1 values for those

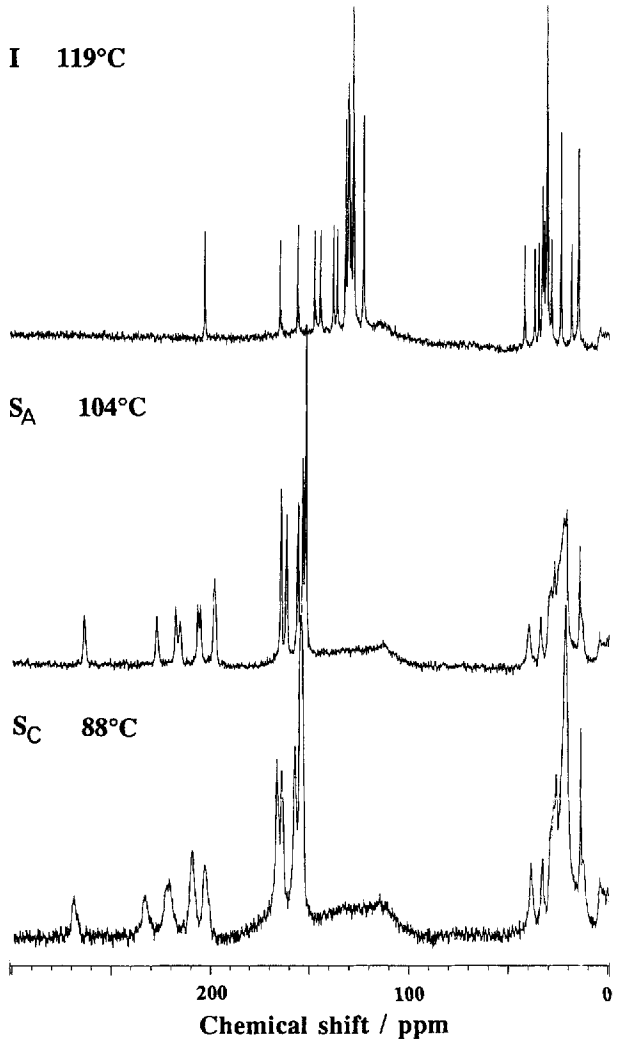

Figure 9. The C-13 NMR spectra of (*S*,*R*)-MONBIC in the isotropic liquid, S_A, and S_C phases without sample spinning.

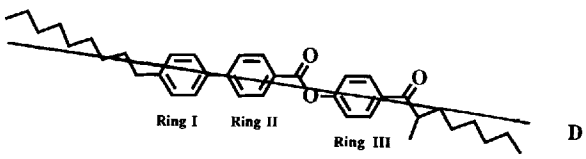

Figure 10. Definition of the molecular long axis, *D*.

carbons. The phase transition was observed by the change of the C-13 NMR spectrum from S_A to S_C^*. The molecular motions in the range from 10^{-12} to 10^{-8} s are effective in C-13 T_1 relaxation. The liquid like C-13 T_1 values listed in table 3 reflect the presence of fast overall motions of an individual molecule of (*S*)-MONBIC in the oriented S_A and S_C^* phases. The overall motions are thought to produce the characteristic mobility responsible for the appearance of the smectic phases [16, 31]. C-13 T_1 decreases along the tail from C_1 to C_9. These results also show that the flexibility decreases on approaching the aromatic core along the tail. The C-13 T_1 of the keto carbon (C_{23}) shows the marked upward deviation near the S_A to S_C^* transition.

Sharp and resolved spectra were obtained for nonoriented (*S*)-MONBIC and (*S*,*R*)-MONBIC in the S_A and S_C^* (S_C) phases by spinning the sample at the magic angle. Figure 11 shows typical C-13 NMR spectra of (*S*)-MONBIC in the S_A and S_C^* phases. The NMR spectrum (see figure 11 (*b*)) did not depend on time. The relative peak intensities observed for C_{20} with decreasing temperature are as follows: 1·00 (122·9 ppm) at 108°C, 1·01 (122·9 ppm) at 106°C, 1·06 (122·9 ppm) at 104°C, 0·93 (123·0 ppm) and a shoulder peak at 102°C, 0·71 (123·0 ppm) and 0·41 (123·6 ppm) at 100°C, 0·90 (123·6 ppm) at 98°C, 0·90 (123·6 ppm) at 96°C, and 0·88 (123·6 ppm) at 94°C. These values indicate that there are differences in chemical shifts for two phases with MAS. During the phase transition from S_A to S_C^*, the lines for all of the core and aliphatic carbons of (*S*)-MONBIC become slightly broader, and the chemical shifts of the core carbons increase. The line broadenings and downfield shifts for (*S*,*R*)-MONBIC also occur at the S_A to S_C transition with MAS.

The measurements of C-13 T_1 for individual carbon atoms of the compounds were carried out under the MAS condition. The results obtained for (*S*)-MONBIC are listed in table 4, C-13 T_1 values of the carbons for (*S*)-MONBIC in the S_A phase show a similar tendency compared with those in the isotropic liquid phase and those in chloroform solution. This similar tendency means that intermolecular interactions affect fast molecular motions slightly in the S_A phase. C-13 T_1 values of C_{10} with the neighbouring methylene protons are shorter than those of C_{13}, C_{14}, C_{19}, and C_{22}. C-13 T_1 values of C_{23} with the neighbouring methyne proton are shorter than those of C_{18}. Except for the S_A to S_C^* transition, the temperature dependence of C-13 T_1 values of C_9 and unprotonated carbons in the S_C^* phase is different from that in the S_A phase. This difference suggests that intermolecular interaction in the S_C^* phase contributes to the mobility of the molecule. The temperature dependence of C-13 T_1 of the protonated aromatic and unprotonated carbons of (*S*)-MONBIC in the S_A and S_C^* phases is shown in figure 12. During the phase transition

Table 3. C-13 T_1 (s) for (*S*)-MONBIC in the S_A and S_C^* phases without sample spinning.

Temperature/°C		C_1	C_9	C_{20}	C_{23}	C_{24}
S_A	110	8·0	0·6	2·1	7·5	0·7
	106	7·1	0·5	1·0	9·5	0·4
	103	6·5	0·4	0·6	18	0·5
S_C^*	100	5·9	—	—	35	0·6
	94	5·5	—	—	14	0·9
	90	5·9	0·7	—	6·4	—

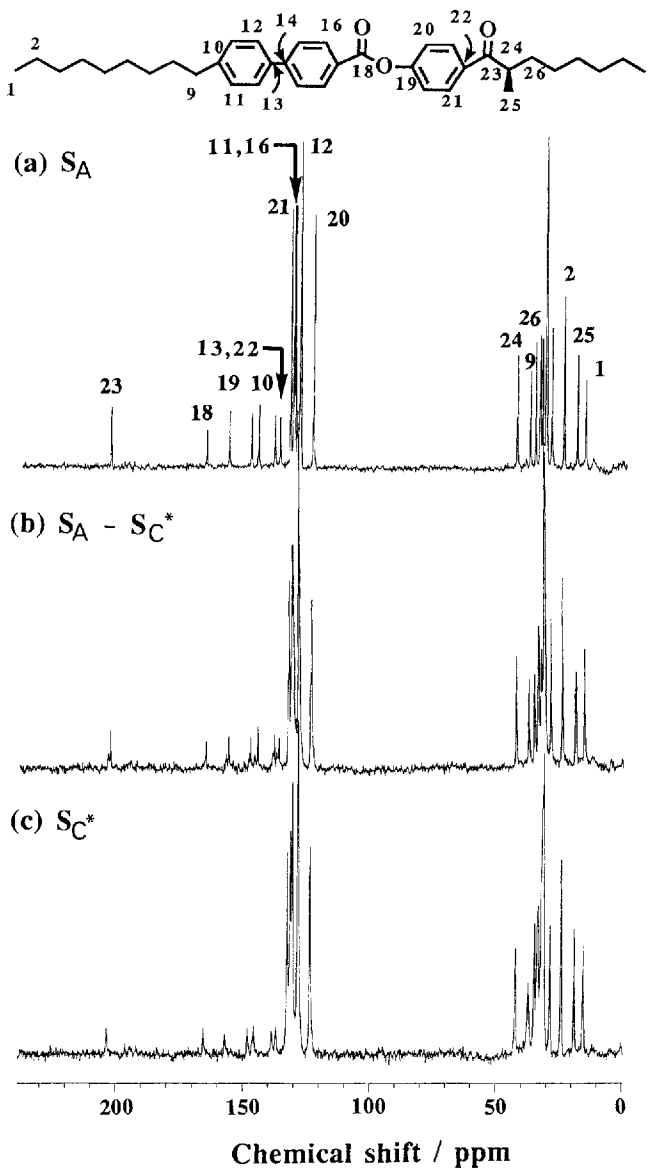

Figure 11. The C-13 NMR spectra of (*S*)-MONBIC (*a*) in the S_A phase (112°C), (*b*) at the S_A–S_C^* coexistence (100°C), and (*c*) in the S_C^* phase (96°C) with sample spinning.

from S_A to S_C^*, there is the decrease in C-13 T_1 of some carbons in the S_A phase near the S_A to S_C^* transition (see table 4). The phase transition was confirmed by the change of C-13 NMR spectrum from S_A to S_C^*. Then, there is the increase in C-13 T_1 of certain carbons at the transition (see table 4 and figure 12). The observed fluctuations of C-13 T_1 values of these carbons near the transition are larger than the experimental error. At the S_A–S_C^* coexistence as shown in figure 10 (*b*), the C-13 T_1 values of the aromatic carbon (C_{20}) in the S_A and S_C^* phase are 329 ms and 471 ms, respectively. The marked increase in C-13 T_1 of the unprotonated carbons of nonoriented (*S*)-MONBIC agrees with that of the keto carbon of oriented (*S*)-MONBIC observed by static C-13 NMR (see table 3). The temperature dependence of C-13 T_1 for (*S*,*R*)-MONBIC is similar to that for (*S*)-MONBIC. C-13 T_1 values for (*S*,*R*)-MONBIC in the S_A and S_C phases are listed in table 5. The fluctuations of C-13 T_1 of certain carbons of (*S*,*R*)-MONBIC were also observed near the S_A to S_C transition. The results of C-13 T_1 measurements suggest that there is no significant difference in fast motions between (*S*)-MONBIC and (*S*,*R*)-MONBIC. This is consistent with the dependence of spontaneous polarization on optical purity.

We interpret the obvious jumps in the T_1 values of the unprotonated carbons and the fluctuations of the T_1 values of some protonated carbons near the S_A to S_C^* transition. The carbon is relaxed by its dipole–dipole interaction with the bound proton. At high fields, the contribution of chemical shift anisotropy to C-13 relaxation is significant, especially for unprotonated carbons. Although the contribution is estimated to be small under the MAS condition, the present MAS condition (4·5 kHz) is not fast enough to reduce its effect on faster relaxation completely. In order to know the change in the dipole–dipole interaction near the transition, we measured the nuclear Overhauser enhancement (NOE) ratio in the S_A and S_C^* phases under the MAS condition. Using the T_1 data and the NOE ratio, the dipolar relaxation time (T_{1D}) can according to the equation [32]

$$1/T_{1D} = (\mathrm{NOE} - 1)/1{\cdot}988\, T_1. \qquad (5)$$

The T_1 data, the NOE ratio, and the T_{1D} data thus calculated are listed in table 6. The T_{1D} excludes the contribution from the chemical shift anisotropy. The values of T_1 (at 98°C)/T_1 (at 108°C) for C_{23} and T_{1D} (at 98°C)/T_{1D} (at 108°C) for C_{23} are 3·5 and 3·7, respectively. A comparison of the T_1 values versus the T_{1D} values indicates that: (1) the relaxation mechanism for the protonated carbons of (*S*)-MONBIC can be assumed to be the dipole–dipole interaction, (2) the change in the dipole–dipole interaction near the transition causes the jumps in the T_1 values of the unprotonated carbons, and (3) the observed increase in the T_1 values of the unprotonated carbons from S_A to S_C^* except for the jumps near the transition is not contributed by the dipole–dipole interaction. Therefore, we can analyse the T_1 data of (*S*)-MONBIC near the transition based on the dipole–dipole relaxation mechanism. C-13 spin-lattice relaxation time for the two spin system may be expressed as follows:

$$1/T_1 = [\gamma_C^2 \gamma_H^2 \hbar^2/16r^6][J_0(\omega_H - \omega_C) + 18J_1(\omega_C) + 9J_2(\omega_H + \omega_C)] \qquad (6)$$

assuming the magnetic dipole–dipole interaction between the two spins as a main cause of the relaxation. Here, γ_C,

γ_H and ω_C, ω_H denote the corresponding gyromagnetic ratios and Larmor frequencies of ^{13}C and ^1H, respectively. r is the internuclear distance between ^{13}C and ^1H. The spectral densities $J_m(\omega)$ are defined to be the Fourier transforms of the correlation functions of the orientation functions (F_m) which are functions of the C–H internuclear vector.

$$J_m(\omega) = \int_{-\infty}^{\infty} \langle F_m^*(t+\tau)F_m(t)\rangle \exp(-i\omega\tau)\, d\tau, \qquad (7)$$

with $m = 0, 1$, and 2, where the angular bracket designates the average of the spin ensemble. The orientation functions F_m are described in terms of spherical harmonics;

$$\left.\begin{aligned} F_0 &= r^{-3}(1 - 3\cos^2\theta), \\ F_1 &= r^{-3}\sin\theta\cos\theta\exp(i\varphi), \\ F_2 &= r^{-3}\sin\theta\exp(2i\varphi). \end{aligned}\right\} \qquad (8)$$

According to the results of table 6, we can assume that the marked jumps in C-13 T_1 values of the unprotonated carbons near the transition are primarily attributed to the change of the dipole–dipole relaxation with neighbouring

Table 4. C-13 T_1 (s) of (*S*)-MONBIC as a function of temperature (°C).

	Protonated aliphatic				
Temperature/°C	C_2	C_9	C_{24}	C_{25}	C_{26}
(I)					
130	4·3	0·5	0·6	2·2	0·8
(S_A)					
112	3·35	0·42	0·57	1·62	0·68
110	3·19	0·42	0·54	1·55	0·68
108	3·18 ± 0·01	0·42 ± 0·02	0·54 ± 0·01	1·51 ± 0·04	0·65 ± 0·01
106	2·65 ± 0·12	0·41 ± 0·01	0·50 ± 0·01	1·40 ± 0·03	0·62 ± 0·03
104	2·40	0·41	0·49	1·31	0·62
102	2·40 ± 0·18	0·40 ± 0·01	0·46 ± 0·01	1·24 ± 0·06	0·51 ± 0·03
100†	2·40	0·38	0·48	1·18	0·45
(S_C^*)					
98	2·49 ± 0·04	0·64	0·51	1·45 ± 0·07	0·66
96	2·39	0·54	0·53	1·42	0·61
94	2·46 ± 0·16	0·66 ± 0·01	0·49 ± 0·02	1·34 ± 0·11	0·59 ± 0·01
92	2·04	0·59	0·45	1·21	0·54
(In $CDCl_3$)					
24	3·8	0·5	0·8	1·4	0·8

	Protonated aromatic				
Temperature/°C	C_{11}	C_{12}	C_{16}	C_{20}	C_{21}
(I)					
130	0·9	0·9	0·6	0·6	0·5
(S_A)					
112	0·76	0·69	0·52	0·51	0·54
110	0·79	0·68	0·51	0·50	0·51
108	0·75 ± 0·01	0·67	0·47 ± 0·01	0·47 ± 0·01	0·50 ± 0·01
106	0·72 ± 0·02	0·65	0·47 ± 0·01	0·46 ± 0·01	0·47 ± 0·01
104	0·70	0·64	0·45	0·46	0·46
102	0·64 ± 0·04	0·55 ± 0·01	0·40 ± 0·02	0·35 ± 0·01	0·41 ± 0·02
100†	0·59	0·53	0·36	0·33	0·35
(S_C^*)					
98	0·60 ± 0·04	0·50 ± 0·01	0·47	0·50	0·48 ± 0·04
96	0·65	0·47	0·47	0·50	0·45
94	0·59 ± 0·01	0·46 ± 0·01	0·39 ± 0·01	0·39 ± 0·01	0·36 ± 0·03
92	0·55	0·44	0·38	0·36	0·34
(In $CDCl_3$)					
24	1·0	1·0	0·6	0·8	0·8

Table 4 (*continued*).

Temperature/°C	Unprotonated aliphatic and aromatic						
	C_{10}	C_{13}	C_{14}	C_{18}	C_{19}	C_{22}	C_{23}
(I)							
130	1·6	2·4	1·9	4·1	2·1	2·2	2·4
(S_A)							
112	1·54	1·90	1·75	3·76	1·69	2·16	2·36
110	1·51	2·18	1·84	4·16	1·89	2·25	2·45
108	1·48 ± 0·07	1·88 ± 0·20	1·70 ± 0·12	3·74 ± 0·04	1·80 ± 0·03	2·08 ± 0·05	2·59 ± 0·28
106	1·58 ± 0·04	1·91 ± 0·15	1·71 ± 0·20	3·99 ± 0·13	1·83 ± 0·11	1·99 ± 0·02	2·30 ± 0·05
104	1·47	1·57	1·64	3·06	1·88	2·10	2·22
102	1·43 ± 0·20	1·83 ± 0·09	1·66 ± 0·10	3·03 ± 0·41	1·83 ± 0·01	2·13 ± 0·01	2·18 ± 0·10
100†	1·41	1·27	1·28	3·63	1·50	1·20	2·27
(S_C^*)							
98	3·58	10·1	5·65	16·6 ± 2·3	7·75	9·72 ± 1·11	9·06 ± 0·25
96	7·20	—	34·6	10·8	20·0	8·60	8·70
94	4·45 ± 0·50	5·65 ± 0·12	4·43 ± 0·57	4·97 ± 0·25	3·58 ± 0·87	3·68 ± 0·31	4·82 ± 0·25
92	3·04	3·72	6·88	3·50	2·72	3·54	6·59
(In $CDCl_3$)							
24	2·9	3·9	3·8	9·6	3·8	4·4	4·9

† The S_A–S_C^* coexistence was observed at 100°C. The C-13 T_1 values at 100° were obtained from the peaks in the S_A phase.

protons. The C-13 T_1 is proportional to r^6. The value of r is not fixed for an unprotonated carbon, thus a marked change in T_1 values of an unprotonated carbon can result from the change in its r value. Powder X-ray diffraction patterns of (*S*)-MONBIC (see figure 4) show that the average intermolecular distance in the smectic layer is about 4 Å, which is longer than the C–H distance between the unprotonated carbon and its intramolecular neighbouring proton. Therefore, the unprotonated carbon may be relaxed by its dipole–dipole interaction with intramolecular neighbouring protons. The jumps in T_1 values of unprotonated carbons of (*S*)-MONBIC observed in the oriented and non-oriented sample may be thought to be attributed to the increase in the internuclear C–H distance between the unprotonated carbon and its intramolecular neighbouring proton, suggesting the discontinuous change in the dynamic behaviour of the core part near the S_A to S_C^* transition. The C-13 relaxation mechanism for unprotonated carbons is complex, thus it seems to be difficult to discuss T_1 values of unprotonated carbons quantitatively without an appropriate model [33].

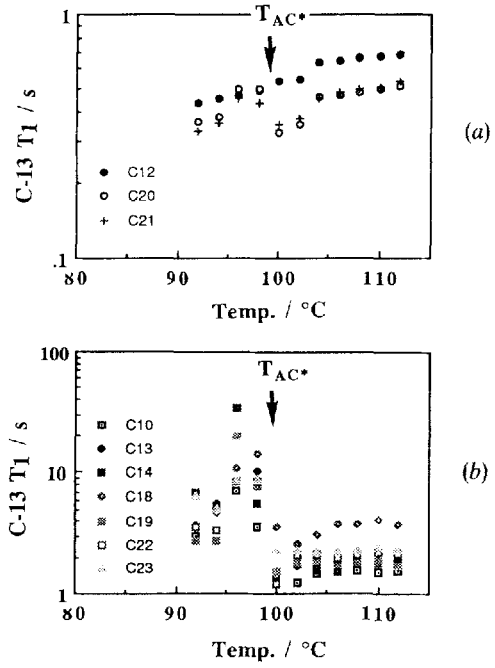

Figure 12. The temperature dependence of C-13 T_1 of (*a*) the protonated-aromatic carbons and (*b*) the unprotonated carbons of (*S*)-MONBIC in S_A and S_C^* phases with MAS.

We analyse the protonated C-13 T_1 for (*S*)-MONBIC. Recently, O'Brien *et al.* [34], have reported the dynamics of molecular reorientations in 4-(2-methyloctanoyl)-4'-biphenyl-3-chloro-4-butyloxybenzoate [31] by using the transient optical Kerr technique. They have detected two kinds of relaxations, i.e. the rotation around the molecular long axis and reorientation of the long axis, in the range from 10^{-11} to 10^{-9} s in the S_A phase near the S_A to S_C^* transition. We can assume that the overall rotation around the long axis and the reorientation of the long axis contribute to C-13 T_1 values. We use the multiple-correlation time model proposed by Murayama *et al.* [35]. The model is shown here briefly. The thermal motion of the C–H vector is described in terms of the superposition of several independent random motions. As shown in

Table 5. C-13 T_1 (s) of (*S*,*R*)-MONBIC in S_A and S_C phases†.

Temperature/°C	C_2	C_9	C_{24}	C_{12}	C_{20}	C_{10}	C_{18}	C_{23}
108 (S_A)	3·21	0·46	0·49	0·62	0·46	1·74	4·49	2·43
103 (S_A)	2·87	0·40	0·46	0·59	0·39	1·58	3·77	2·38
100 (S_A)	—	—	—	—	—	1·42	1·88	1·23
100 (S_C)	2·76	0·39	0·42	0·51	0·60	9·61	22·1	11·4
93 (S_C)	2·64	0·69	0·45	0·44	0·36	4·03	6·11	4·82

† The S_A–S_C coexistence was observed at 100°C. The C-13 T_1 values at 100°C (S_A) and those at 100°C (S_C) were obtained from the peaks in the S_A phase and the peaks in the S_C phase, respectively.

Table 6. NOE, C-13 T_1 (s), and C-13 T_{1d} (s) for (*S*)-MONBIC in the S_A and S_C^* phases with MAS.

	C_{11}			C_{20}			C_{23}		
Temperature/°C	NOE	T_1	T_{1d}	NOE	T_1	T_{1d}	NOE	T_1	T_{1d}
108 (S_A)	2·20	0·75	1·24	2·19	0·47	0·79	1·32	2·59	16·1
98 (S_C^*)	2·35	0·60	0·88	2·34	0·50	0·74	1·30	9·06	60·0
88 (S_C^*)	2·68	0·56	0·66	2·52	0·37	0·48	1·59	3·64	12·3

figure 13, the C–H internuclear vector undergoes the diffusional rotations around the Z_1 axis in frame S_1 with a vertical angle θ_R, and the Z_1 axis librates around another Z_2 axis in frame S_2 within a solid cone of a vertical angle θ_L, and finally, the Z_2 axis undergoes the isotropic random reorientation in the laboratory frame. The correlation times of these motions are τ_R, τ_L, and τ_I, respectively. The motions are described based on the assumptions that, (1) the threefold jump rotation of the C–H vector occurs around the Z_1 axis in frame S_1, and (2) the rapid fluctuation of the Z_1 axis occurring in frame S_2 is described by the librational motion. The orientation functions can be expressed as

$$F_m(t)F_m(t) = \sum_{j,k}^{5} f_{jk}^{(m)}(t)g_{jk}^{(m)}(t)h_{jk}^{(m)}(t). \quad (9)$$

Here $f_{jk}^{(m)}(t)$ are the functions arising from the rotational motion of the C–H vector, and $g_{jk}^{(m)}(t)$ are the functions from the librational motion of the Z_1 axis, and $h_{jk}^{(m)}(t)$ are the functions from the spherical motion of the Z_2 axis. Assuming the motions to be independent of each other, the correlation functions of the orientation functions of the C–H vector can be expressed as

$$\langle F_m^*(t+\tau)F_m(t)\rangle = \sum_{j,k}\sum_{l,n}\langle f_{jk}^{(m)*}(t+\tau)f_{ln}^{(m)}(t)\rangle \times \langle g_{jk}^{(m)*}(t+\tau)g_{ln}^{(m)}(t)\rangle\langle h_{jk}^{(m)*}(t+\tau)h_{ln}^{(m)}(t)\rangle \quad (10)$$

Equation (9) is reduced to the functions of θ_R, θ_L, τ_R, τ_L, and τ_I as [34]

$$\begin{aligned}\langle F_m^*(t+\tau)F_m(t)\rangle = K_m[&A_RA_L\exp(-|\tau|/\tau_1)\\ &+ A_R(1-A_L)\exp(-|\tau|/\tau_1)\\ &+ B_RB_L\exp(-|\tau|/\tau_2)\\ &+ B_R(1-B_L)\exp(-|\tau|/\tau_3)\\ &+ C_RC_L\exp(-|\tau|/\tau_4)\\ &+ C_R(1-C_L)\exp(-|\tau|/\tau_5)], \end{aligned} \quad (11)$$

where

$$A_R = (1/4)(3\cos^2\theta_R - 1)^2,$$
$$B_R = 3\sin^2\theta_R\cos^2\theta_R,$$
$$C_R = (3/4)\sin^2\theta_R,$$
$$A_L = \cos^2\theta_L(1+\cos\theta_L)^2/4,$$
$$B_L = \sin^2\theta_L(1+\cos\theta_L)^2/6,$$
$$C_L = (\cos\theta_L + 2)^2(\cos\theta_L - 1)^2/24,$$

with

$$K_0 = 4/5, \quad K_1 = 2/15, \quad K_2 = 8/15,$$

and

$$\tau_1^{-1} = \tau_L^{-1} + \tau_I^{-1}, \quad \tau_2^{-1} = \tau_R^{-1} + \tau_I^{-1},$$
$$\tau_3^{-1} = \tau_R^{-1} + \tau_L^{-1} + \tau_I^{-1},$$
$$\tau_4^{-1} = 4\tau_R^{-1} + \tau_I^{-1}, \quad \tau_5^{-1} = 4\tau_R^{-1} + \tau_L^{-1} + \tau_I^{-1}.$$

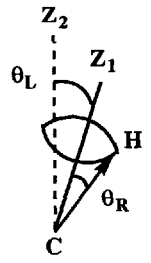

Figure 13. The schematic diagram of the multiple-correlation-time model for the motion of the C–H vector.

Fourier transformation of equation (10) yields the spectral densities as

$$J_m = (\omega) = K_m[A_R A_L 2\tau_1/(1 + \omega^2\tau_1^2) + A_R(1 - A_L)2\tau_1/(1 + \omega^2\tau_1^2) + B_R B_L 2\tau_2/(1 + \omega^2\tau_2^2) + B_R(1 - B_L)2\tau_3/(1 + \omega^2\tau_3^2) + C_R C_L 2\tau_4/(1 + \omega^2\tau_4^2) + C_R(1 - C_L)2\tau_5/(1 + \omega^2\tau_5^2)]. \quad (12)$$

Let us apply the model to the molecular motions of (*S*)-MONBIC in the smectic phases. The rotation of the C–H vector around the Z_1 axis corresponds to the overall molecular rotation around the molecular long axis. θ_R is the angle between the C–H vector and the long axis. The libration of the Z_1 axis around the Z_2 axis corresponds to the reorientation of the long axis around the axis parallel to the layer normal, i.e. the director in the S_A phase. θ_L is the thermal average or the orientational angle of the long axis with respect to the layer normal. θ_L is assumed to be $2 \times 10°$ based on the order parameter of the long axis of (*S*)-MONBIC in the S_A phase. In the anisotropic smectic phases, the isotropic reorientation of the Z_2 axis may not occur and the reorientation of Z_2 axis, for instance, the fluctuation of the director, is too slow to contribute to C-13 T_1 values. Therefore, we can assume $\tau_I = \infty$ in the spectral densities. Lalanne *et al.* have investigated fast individual molecular reorientations in the S_A phase in the vicinity of the S_A to S_C^* transition by means of the degenerate four-waves-mixing technique [36]. The relaxation time of the motion in the S_A phase of ZLI 3488 is estimated to be about 30 ps. Following the report by O'Brien *et al.* [34], the relaxation time of the reorientation around the molecular long axis is smaller than 55 ps and that of the reorientation of the long axis is a few ns. We can assume that τ_R and τ_L in the multiple-correlation-time model are 1×10^{-11} s and 1×10^{-9} s, respectively. We examine the dependence of the protonated aromatic C-13 T_1 for (*S*)-MONBIC on the parameters. The flip–flop motion of each aromatic ring of (*S*)-MONBIC can be assumed to be much slower than the overall rotation around the long axis and the reorientation of the long axis. According to the definition of the long axis, the angle of the C–H vector for the protonated aromatic carbon with respect to the long axis is thought to be about 50° or 70°. Therefore, θ_R for C_{20} and θ_R for C_{21} can be assumed to 50° and 70°, respectively. We use $\tau_R = 1 \times 10^{-11}$ s, $\tau_L 1 \times 10^{-9}$ s, $\theta_R = 5 \times 10°$, and $\theta_L = 2 \times 10°$ as initial values. The parameter dependence of the C-13 T_1 calculated from the model is shown in figure 14. Figure 14 (*a*) shows the calculated dependence of C-13 T_1 of a protonated aromatic carbon of τ_R, where $\theta_R = 50°$, $\theta_L = 20°$, and $\tau_L = 10^{-9}$ s, and that on τ_L, where $\theta_R = 50°$, $\theta_L = 20°$, and

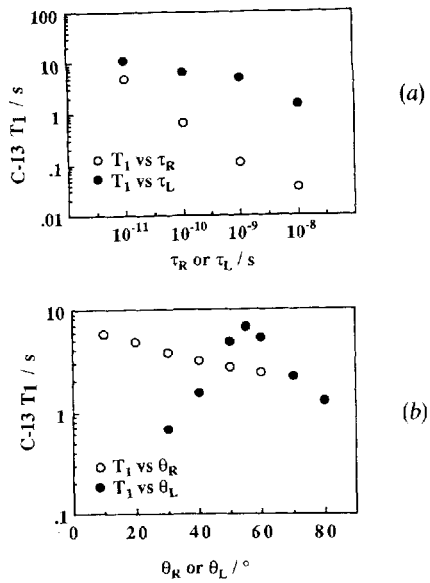

Figure 14. The calculated dependence of a protonated aromatic C-13 T_1 on (*a*) τ_R or τ_L, and (*b*) θ_R or θ_L.

$\tau_R = 10^{-11}$ s. Figure 14 (*b*) shows the calculated dependence of C-13 T_1 of a protonated aromatic carbon on θ_R where $\tau_R = 10^{-11}$ s, $\tau_L = 10^{-9}$ s, and $\theta_L = 20°$, and that on θ_L where $\tau_R = 10^{-11}$ s, $\tau_L = 10^{-9}$ s, and $\theta_R = 50°$. In the case of $\theta_R = 70°$, calculated C-13 T_1 values also decrease with either the increase of τ_R, the increase of τ_L, or the increase of θ_L. Figure 14 (*b*) shows that calculated C-13 T_1 values of C_{20} with $\theta_R = 50°$ increase with the increase of θ_R and calculated C-13 T_1 values of C_{21} with $\theta_R = 70°$ increase with the decrease of θ_R. The results of figure 14 (*b*) are consistent with the definition of the long axis shown in figure 10, for instance, the increase of θ_R for C_{20} causes the decrease of θ_R for C_{21}. Although there is still significant difference in values between the calculated T_1 and the observed T_1, we can get qualitative information from the results of figure 14. As shown in figure 12 (*a*), C-13 T_1 values of C_{20} and C_{21} in the ring III increase at the S_A to S_C^* transition, but those of C_{12} in ring I do not show such an increase at the transition (see also table 4). The temperature dependent C-13 T_1 values of those carbons of (*S*,*R*)-MONBIC at the S_A to S_C are similar to those of (*S*)-MONBIC at the S_A to S_C^* transition (see table 5). According to figure 14, the increase in C-13 T_1 can result from either the decrease in τ_L, the decrease in τ_R, the decrease in θ_L, or the change in θ_R (see also figure 15). Either the change in the correlation times of the overall motions, i.e. the rotation around the long axis and the reorientation of the long axis, or the change in the tilt angle of the long axis may not cause the different behaviour in C-13 T_1 values among C_{12}, C_{20}, and C_{21}. The decrease in τ_R, i.e. the overall rotation around the long axis becomes faster, as decreasing temperature is unrealistic. The

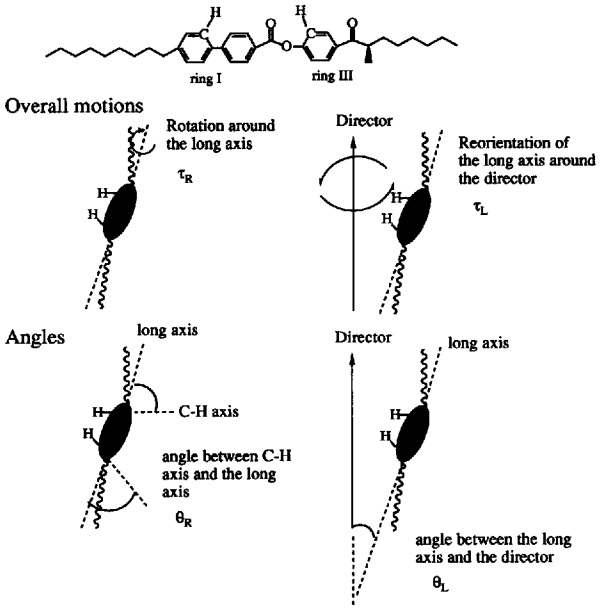

Figure 15. The factors that may effect C-13 T_1 values.

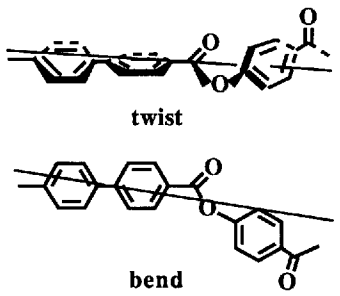

Figure 16. The molecular deformation for the core part. The estimated long axis is shown.

decrease in θ_L, i.e. the decrease in a molecular tilt, at the S_A to S_C^* transition is also unrealistic. Therefore, the fluctuation of C-13 T_1 values observed near the transition can be attributed to the change of θ_R, i.e. the change of the angle between the C–H vector and the long axis. The difference between C_{20} and C_{12} in the temperature dependence of C-13 T_1 values near the transition can be interpreted as following. The change of the angle between the long axis and the C–H axis in the ring III is thought to be larger than that in the ring I at the transition. This can result from the molecular deformation—twist or bend—for the core part as shown in figure 16. The molecular deformation is consistent with the different tendency in the orientation with respect to the magnetic field among the phenyl rings observed by static C-13 NMR near the transition (see table 2). The molecular deformation may cause the change of the internuclear C–H distance between the unprotonated carbon and its intramolecular neighbouring proton of (*S*)-MONBIC, which affects C-13 T_1 values of unprotonated carbons. Thus, the results of C-13 NMR measurements indicate that the dynamic molecular deformation occurs near the S_A to S_C^* transition. Figure 14 (*a*) also gives information concerning the overall rotation around the molecular long axis. According to figure 14 (*a*), C-13 T_1 decreases remarkably with the increase in τ_R. There is no marked decrease in C-13 T_1 values of the protonated aromatic carbon from S_A to S_C^* as shown in table 4. This indicates the absence of the slowing down of the molecular rotation around the long axis at the S_A to S_C^* transition, which is in agreement with our previous C-13 CP/MAS NMR work [16, 17] and with the recent time-resolved FT-IR work [37]. Our results support the dielectric spectroscopy experiments reported by Vallerien and Kremer *et al.* [38, 39], as well as the transient Kerr experiments reported by O'Brien *et al.* [34]. The slowing down of the rotation around the long axis reported by Lalanne *et al.* [36, 40], was not detected by our C-13 NMR study.

C-13 $T_{1\rho}$ measurements with MAS were performed for nonoriented (*S*)-MONBIC and (*S*, *R*)-MONBIC in the smectic phases. The motions in the range 10^{-6} to 10^{-4} s are effective in C-13 $T_{1\rho}$. C-13 $T_{1\rho}$ values of protonated and unprotonated carbons of the core for (*S*)-MONBIC were obtained (see table 7). The temperature dependence of C-13 $T_{1\rho}$ for (*S*)-MONBIC was similar to that for (*S*, *R*)-MONBIC. C-13 $T_{1\rho}$ values decrease near the transition. On the other hand, C-13 $T_{1\rho}$ of protonated aliphatic carbons could not be obtained in the smectic phases, i.e. motion in the range from 10^{-6} to 10^{-4} s was not detected for the tails. Since we do not have enough information about motions which are effective in C-13 $T_{1\rho}$, we cannot interpret the results of C-13 $T_{1\rho}$ measurements according to an appropriate model. Therefore, based on the simple treatment, we evaluate the correlation time of the motion for the molecular core from C-13 $T_{1\rho}$ values of the protonated aromatic carbon (C_{21}) of (*S*)-MONBIC. C-13 $T_{1\rho}$ is expressed by [41]

$$1/T_{1\rho} = (1/2)M_{CH}^{(2)} \times 2\tau_c/(1 + \omega_{1c}^2\tau_c^2), \qquad (13)$$

where $\omega_{1c} = 2\pi\upsilon_{1c}$ and $M_{CH}^{(2)}$ is the Van Vleck second moment in rad^2 s^{-2} for the carbon–proton interaction [42]. We assume $\omega_{1c}\tau_c > 1$. Using C-13 $T_{1\rho} = 1$ ms observed for C_{21} of (*S*)-MONBIC in the S_A phase, $\upsilon_{1c} = 56$ kHz, and $M_{CH}^{(2)} = 10^{10}$ rad^2 s^{-2}, the value of τ_c is calculated to be 1×10^{-4} s. The correlation time range of the motion is similar to that of the order fluctuation of the director for ferroelectric liquid crystals observed by measurements of the proton spin relaxation [43]. Dong *et al.* reported the decrease in the proton $T_{1\rho}$ in the nematic phase near the nematic to isotropic liquid transition [44]. C-13 $T_{1\rho}$ values obtained may reflect the fluctuation of the director in the smectic phases. C-13 $T_{1\rho}$ values at 90°C in the S_C^* phase

Table 7. C-13 $T_{1\rho}$ (ms) for (*S*,)-MONBIC in the S_A and S_C^* phases with MAS†.

Temperature/°C	C_{10}	C_{18}	C_{21}	C_{22}	C_{23}
S_A					
110	0·32 (0·29)	0·29 (0·23)	1·33 (1·08)	0·33 (0·28)	0·45 (0·48)
105	0·29	0·24	1·34	0·31	0·40
100‡	0·10	0·09	0·30	0·11	0·13
S_C^* (S_C)					
95	0·14	0·13	0·48	0·16	0·14
90	0·13 (0·10)	0·14 (0·13)	0·49 (0·86)	0·15 (0·12)	0·17 (0·15)

† The values in parentheses are C-13 $T_{1\rho}$ (ms) for (*S*,*R*)-MONBIC in the S_A and S_C phases with MAS.
‡ The S_A–S_C^* coexistence was observed at 100°C. The C-13 $T_{1\rho}$ values were obtained from the peaks in the S_A phase.

are shorter than those at 110°C in the S_A phase, indicating that the fluctuation of the director in the S_C^* phase is larger than that in the S_A phase. Our C-13 $T_{13\rho}$ measurements indicate that: (1) the molecular motion in the correlation time of 10^{-4} s for the core part contributes to the fluctuation of the director, and (2) the marked decrease in C-13 $T_{1\rho}$ in the S_A phase in the vicinity of the S_A to S_C^* transition results from the reorientation of the director. The results of C-13 $T_{1\rho}$ measurements are consistent both with the discontinuous change of static C-13 NMR lines for the core carbons at the S_A to S_C^* transition and with the dynamic molecular deformation near the transition suggested by analysis of C-13 T_1. There is no significant difference in the motions detected by C-13 T_1 and $T_{1\rho}$ between (*S*)-MONBIC and (*S*,*R*)-MONBIC. This is in agreement with a proton spin relaxation study reported by Bender *et al.* [43].

3.4. *A possible S_A to S_C^* transition model*

The results of powder X-ray diffraction and solid-state C-13 NMR measurements allow us to propose a possible S_A–S_C^* transition model. Figure 17 shows the schematic representation of molecular orientation of (*S*)-MONBIC in the S_A and S_C^* phases.

The tails are thought to be disordered in the S_A and S_C^* phases. The orientational angle of the tail with respect to the layer normal decreases slightly in the S_A and S_C^* phases as decreasing temperature. On the other hand, the orientational angle of the core with respect to the layer normal decreases in the S_A phase and increases in the S_C^* phase as the temperature decreases. The orientation of the core part changes discontinuously at the S_A to S_C^* transition. The dynamic molecular deformation for the core part can be thought to occur near the transition. In the S_C^* phase the core parts form the helicoidal layer structure. Let us discuss the origin of the long range correlation of the director in the smectic phases. Figure 18 shows the dynamic molecular deformation effect on the director reorientation near the S_A to S_C^* transition. In the S_A phase the core part may orient around the layer normal with the orientational angle whereas the positional order of the tail in the layer is thought to be free. The orientational angle between the core and the layer normal decreases as the temperature decreases. This means an increase in the density and also a decrease in the intermolecular distance in each layer with a decrease of temperature. Therefore, the intermolecular interaction, for instance, quadrupole–quadrupole interaction, can increase in the S_A phase as the temperature decreases. The interaction may cause the molecular deformation for the core part, which increases the excluded volume of the core part (see also figure 16). In order to minimize the increase in the excluded volume, the reorientation of the core part may occur. As a consequence of this reorientation, the core parts are tilted to a same direction in each layer. The reorientation of the core part can produce the positional order of the tail around the layer normal. This positional order formed in each layer is thought to produce the long range correlation of the direction of the core part over the layers. In the chiral system, the relative orientation of the chiral tail with

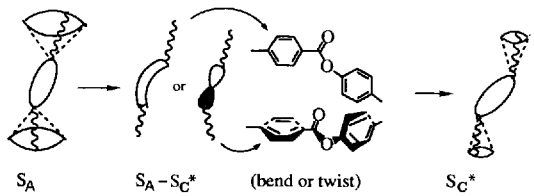

Figure 17. The schematic representation of the molecular orientation of (*S*)-MONBIC in the S_A and S_C^* phases.

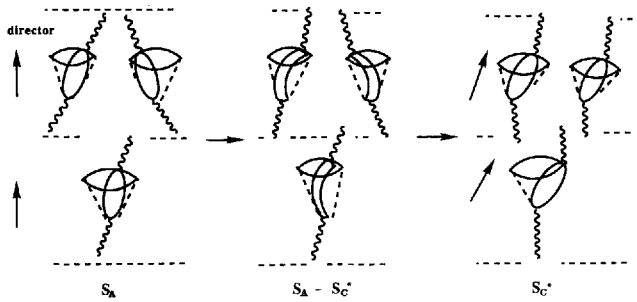

Figure 18. The dynamic molecular deformation effect on the reorientation of the director near the S_A to S_C^* transition.

respect to the core part depends on the absolute configuration of the chiral centre and the steric hindrance. The interlayer permeation of the chiral tail may cause twist interaction between the cores in adjacent layers. As a result from the twist interaction, the core parts form to the helicoidal layer structure in the S_C^* phase. This twist mechanism is supported by our recent chiral system, i.e. strong helical structures produced by chiral twin compounds [45]. Then, the reported experimental results by Coates [46] and us [47] that the introduction of a lateral substituent to the position of C_{20} markedly depress the S_A to S_C^* transition temperature can be explained by the present dynamic molecular deformation effect on the S_A to S_C^* transition. The bend or twist of ring III is thought to be hard to occur by the introduction of the substituent to the position of ring III.

4. Conclusions

We detected the discontinuous change in the orientation and dynamics of the core part at the S_A to S_C^* transition by means of solid-state C-13 NMR. Analysis of C-13 T_1 reveals that the dynamic molecular deformation for the core part may occur near the transition. The results of C-13 NMR, X-ray, and electro-optical measurements allow us to propose the structural model which describes the microscopic organization of the molecules in the S_A and S_C^* (S_C) phases. The model indicates that the dynamic molecular deformation which cannot be described by a static rod model plays an important role in the reorientation of the director at the S_A to S_C^* transition. We present here one example of the correlation between orientational order in the chiral smectic phases and microscopic behaviour of an individual molecule. The orientation and motion of an individual molecule discussed in this paper are affected by the molecular structure. The correlation between molecular structure and dynamic behaviour of the molecule in the smectic phases is now investigated.

We would like to thank Dr T. Fujito of JEOL Ltd. for providing the pulse sequence for C-13 $T_{1\rho}$ measurements. We acknowledge Mr K. Yoshida for obtaining the X-ray patterns and Miss N. Ise for electro-optical measurements. We are also grateful to Dr I. Nishiyama for stimulating discussions.

References

[1] GRAY, G. W., and GOODBY, J. W., 1984, *Smectic Liquid Crystals: Textures and Structures* (Leonard-Hill).

[2] MEYER, R. B., LIEBERT, L., STRZELECKI, L., and KELLER, P., 1975, *J. Phys. Lett., Paris*, **36,** L69.

[3] GOODBY, J. W., WAUGH, M. A., STEIN, S. M., CHIN, E., PINDAK, R., and PATEL, J. S., 1989, *J. Am. chem. Soc.*, **111,** 8119.

[4] (a) CHANDANI, A. D. L., GORECKA, E., OUCHI, Y., TAKEZOE, H., and FUKUDA, A., 1989, *Jap. J. appl. Phys.*, **28,** L1265. (b) GALERNE, Y., and LIEBERT, L., 1989, *Second International Conference of Ferroelectric Liquid Crystals, 27–30 June, Göteborg, Sweden*, O-27.

[5] (a) WALBA, D. M., SLATER, S. C., THURMES, W., CLARK, N. A., HANDSCHY, M. A., and SUPON, F., 1986, *J. Am. chem. Soc.*, **108,** 5210. (b) WALBA, D. M., RAZAVI, H. A., HORIUCHI, A., EIDMAN, K. F., OTTERHOLM, B., HALTIWANGER, R. C., CLARK, N. A., SHAO, R., PARMAR, D. S., WAND, M. D., and VOHRA, R. T.., 1991, *Ferroelectrics*, **113,** 21.

[6] (a) GOODBY, J. W., and LESLIE, T. M., 1984, *Molec. Crystals liq. Crystals*, **110,** 175. (b) GOODBY, J. W., 1991, *J. mater. Chem.*, **1,** 307.

[7] TAKEZOE, H., FUKUDA, A., IKEDA, A., TAKANISHI, Y., UMEMOTO, T., WATANABE, J., IWANE, A., HARA, M., and ITOH, K., 1991, *Ferroelectrics*, **122,** 167.

[8] VAN DER MEER, B. W., and VERTOGEN, G., 1979, *J. Phys., Paris*, **40,** C3-222.

[9] GOOSSENS, W. J. A., 1987, *Molec. Crystals liq Crystals*, **150,** 419.

[10] NAKAGAWA, M., 1987, *Liq. Crystals*, **3,** 573.

[11] DE GENNES, P. G., 1974, *The Physics of Liquid Crystals* (Clarendon Press).

[12] BLINC, R., FILIPIC, C., LEVSTIK, A., ZEKS, B., and CARLSON, T., 1987, *Molec. Crystals liq. Crystals*, **151,** 1.

[13] PINES, A., and CHANG, J. J., 1974, *Phys. Rev.* A, **10,** 946.

[14] LUZAR, M., RUTAR, V., SELIGER, J., and BLINC, R., 1984, *Ferroelectrics*, **58,** 115.

[15] POON, C. D., and FUNG, B. M., 1989, *J. chem. Phys.*, **91,** 7392.

[16] YOSHIZAWA, A., KIKUZAKI, H., HIRAI, T., and YAMANE, M., 1989, *Jap. J. appl. Phys.*, **28,** L1988.

[17] YOSHIZAWA, A., KIKUZAKI, H., HIRAI, T., and YAMANE, M., 1990, *Jap. J. appl. Phys.*, **29,** L1153.

[18] YOSHIZAWA, A., NISHIYAMA, I., KIKUZAKI, H., and ISE, N., 1992, *Jap. J. appl Phys.*, **31,** L860.

[19] MIYASATO, K., ABE, S., TAKEZOE, H., FUKUDA, A., and KUZE, E., 1983, *Jap. J. appl. Phys.*, **22,** L661.

[20] LEADBETTER, A. J., 1979, *The Molecular Physics of Liquid Crystals*, edited by G. R. Luckhurst and G. W. Gray (Academic Press), Chap. 13.

[21] (a) BARTOLINO, R., DOUCET, J., and DURAND, G., 1978, *Ann. Phys.*, **3,** 389, (b) MARTINOT-LAGARDE, PH., DUKE, R., and DURAND, G., 1981, *Molec. Crystals liq. Crystals*, **75,** 249.

[22] GOODBY, J. W., CHIN, E., LESLIE, T. M., GEARY, J. M., and PATEL, J. S., 1986, *J. Am. chem. Soc.*, **108,** 4729.

[23] YOSHIZAWA, A., NISHIYAMA, I., FUKUMASA, M., HIRAI, T., and YAMANE, M., 1989, *Jap. J. appl. Phys.*, **28,** L1269.

[24] YOSHIZAWA, A., YOKOYAMA, A., KIKUZAKI, H., and HIRAI, T., 1993, *Liq. Crystals*, **14,** 513.

[25] SAFINYA, C. R., KAPLAN, M., ALS-NIELSEN, J., BIRGENEAU, R. J., DAVIDOV, D., LITSTER, J. D., JOHNSON, D. L., and NEUBERT, M. E., 1980, *Phys. Rev.* B, **21,** 4149.

[26] BURUM, D. P., LINDER, N., and ERNST, R. R., 1981, *J. magn. Reson.*, **44,** 173.

[27] ADAMS, J. M., and MORSI, S. E., 1976, *Acta Crystallogr.* B, **32,** 1345.

[28] OULYADI, H., LAUPRÊTE, L., MOMMERIE, L., MAUZAC, M., RICHARD, H., and GASPAROUX, H., 1990, *Macromolecules*, **23,** 1965.

[29] WEMMER, D. E., PINES, A., and WHITEHURST, D. D., 1981, *Phil. Trans. R. Soc.* A, **300,** 15.

[30] MARICQ, M. M., and WAUGH, J. S., 1979, *J. chem. Phys.*, **70,** 3300.

[31] YOSHIZAWA, A., YOKOYAMA, A., and NISHIYAMA, I., 1992, *Liq. Crystals*, **11,** 235.
[32] ALGER, T. D., COLLINS, S. W., and GRANT, D. M., 1971, *J. chem. Phys.*, **54,** 2970.
[33] WITTEBORT, R. J., SUBRAMANIAN, R., KULSHRESHTHA, N. P., and DUPRÉ, D. B., 1985, *J. chem. Phys.*, **83,** 2457.
[34] O'BRIEN, J. P., MOSES, T., CHEN, E., FREYSZ, E., OUCHI, Y., and SHEN, Y. R., 1993, *Phys. Rev.* E, **47,** R2269.
[35] MURAYAMA, K., HORII, F., and KITAMARU, R., 1983, *Bull. Inst. chem. Res. Kyoto Univ.*, **61,** 229.
[36] LALANNE, J. R., DESTRADE, H., NGUYEN, H., and MARCEROU, J. P., 1991, *Phys. Rev.* A, **44,** 6632.
[37] MASUTANI, K., YOKOTA, A., FURUKAWA, Y., TASUMI, M., and YOSHIZAWA, A., 1993, *Appl. Spectrosc*, **47,** 1370.
[38] VALLERIEN, S. U., KREMER, F., KAPITZA, H., ZENTEL, R., and FRANK, W., 1989, *Physics Lett.* A, **138,** 219.
[39] KREMER, F., VALLERIEN, S. U., KAPITZA, R., ZENTEL, R., and FISCHER, E. W., 1990, *Phys. Rev.* A, **42,** 3667.
[40] LALANNE, J. R., BUCHERT, J., DESTRADE, C., NGUYEN, H. T., and MARCEROU, J.P., 1989, *Phys. Rev. Lett.*, **62,** 3046.
[41] VANDERHART, D. L., and GARROWAY, A. N., 1979, *J. chem. Phys.*, **71,** 2773.
[42] VAN VLECK, J. H., 1948, *Phys. Rev.*, **70,** 1168.
[43] BENDER, H., NOACK, F., VILFAN, M., and BLINC, R., 1989, *Liq. Crystals*, **5,** 1233.
[44] DONG, R. Y., and TOMCHUK, E., 1978, *Phys. Rev.* A, **17,** 2062.
[45] YOSHIZAWA, A., and NISHIYAMA, I., 1994, *J. mater. Chem.*, **4,** 449.
[46] COATES, D., 1987, *Liq. Crystals*, **2,** 432.
[47] HIRAI, T., FUKUMASA, M., NISHIYAMA, I., YOSHIZAWA, A., SHIRATORI, N., YOKOYAMA, A., and YAMANE, M., 1991, *Ferroelectrics*, **114,** 251.